



CHORUS

This is the accepted manuscript made available via CHORUS. The article has been published as:

Harnessing the photonic local density of states in graphene moiré superlattices

W. J. M. Kort-Kamp, F. J. Culchac, F. S. S. Rosa, C. Farina, Rodrigo B. Capaz, and F. A. Pinheiro

Phys. Rev. B **103**, 155423 — Published 26 April 2021

DOI: [10.1103/PhysRevB.103.155423](https://doi.org/10.1103/PhysRevB.103.155423)

Harnessing the photonic local density of states in graphene Moiré superlattices

W. J. M. Kort-Kamp,¹ F. J. Culchac,² F. S. S. Rosa,² C. Farina,² Rodrigo B. Capaz,² and F. A. Pinheiro²

¹*Theoretical Division, MS B262, Los Alamos National Laboratory, Los Alamos, New Mexico 87545, United States**

²*Instituto de Física, Universidade Federal do Rio de Janeiro, Caixa Postal 68528, Rio de Janeiro 21941-972, RJ, Brazil[†]*

(Dated: April 8, 2021)

In this work we investigate the electromagnetic local density of states (LDOS) near of a twisted bilayer graphene (TBG) deposited over a general isotropic substrate. The band structure of the TBG is calculated within a tight-binding framework, and then used to determine the TBG's conductivity. The latter presents a non-trivial dependence upon the angle of twist, which shows up in the LDOS, allowing for a Moiré pattern-dependent quantum emission. For some specific twist angles we show that it is possible to either enhance or decrease the LDOS by an order of magnitude at selected frequencies when compared to the monolayer. This impressive variation is explained in terms of the presence/absence of well defined surface plasmon-polaritons (SPPs). Altogether our findings demonstrate that TBG is an alternative, versatile material platform for controlling spontaneous emission and enhancing light-matter interactions, and pave the way for further studies and applications of quantum emission in the emerging class of 2D Moiré materials.

I. INTRODUCTION

In addition to graphene, which has been extensively studied over the past decade¹, two different classes of van der Waals materials have drawn a lot of attention in recent years. One of them is the class of two-dimensional graphene-like materials, produced by exfoliating down materials such as hexagonal boron nitride, molybdenum disulphide, and other dichalcogenides². Another class is composed of two-dimensional crystals assembled together layer by layer with controllable sequence and orientation. These structures exhibit unusual physical properties that cannot be found in monolayers or in bulk². Twisted bilayer graphene (TBG) is one important example of these structures, where the rotation between the two layers produces a Moiré pattern and induces a static periodic potential from the coupling between graphene layers, leading to an angle-dependent band structure³. TBG can occur naturally by chemical vapor deposition growth on metals⁴⁻⁶ or fabricated by mechanically folding graphene⁸ and stacking two monolayers together⁹. TBG has remarkable electronic and optical properties, such as Dirac-like spectrum¹⁰, low energy van Hove singularities^{7,11}, localization of low energy states¹², all of which angle-dependent.

Very recently, the observation of unconventional superconductivity in TBG has triggered an enormous amount of interest in this material^{13,14}. This remarkable result, which is the first evidence of a purely carbon-based 2D superconductor, occurs for some specific “magic” twist angles between the two graphene layers. At these angles TBGs exhibit ultraflat bands near charge neutrality, leading to correlated insulating states. Upon electrostatic doping away from these correlated insulating states, superconductor phases exist with a phase diagram similar to that of cuprates^{13,14}. Altogether, these recent findings indicate that TBG is a new, tunable, and versatile material platform to probe strongly correlated phenomena. Moreover, from the applied point of view, twisting of bilayer graphene allows for the modulation for electronic devices^{15,16}. In addition to TBG, other 2D materials such as MoSe₂/WSe₂ heterobilayers, exhibit Moiré patterns that, by generating an

array of nanoscale electrostatic potential, can trap quasiparticles including excitons. Indeed, optical emission from Moiré-trapped excitons has been recently observed¹⁷⁻²⁰, confirming theoretical predictions²¹.

Despite the considerable recent interest in TBG, its capacity to mediate light-matter interactions at the nanoscale has never been investigated so far. Indeed, despite 2D materials²² being now established platforms to enhance and control spontaneous emission from quantum emitters (atoms, molecules and quantum dots)²³⁻²⁸, this possibility has never been investigated for TBG to the best of our knowledge. The purpose of the present paper is hence to fill this gap by calculating the photonic density of states of TBG using tight-binding methods.

This paper is organized as follows. Section II is devoted to the methodology, where the photonic density of states is calculated in terms of the optical conductivity of TBG, which in turn is given by the tight-binding method. In Section III we present and discuss our main findings whereas Section IV is devoted to the conclusions.

II. METHODOLOGY

A. Photonic Local Density of States

We consider a system where a twisted bilayer graphene is placed atop a substrate, as shown in Fig. 1. The photonic local density of states (LDOS) associated to two-level quantum emitter at position \mathbf{r}_0 in the vicinities of a generic arrangement of objects is given by^{29,30}

$$\rho(\mathbf{r}_0, \omega) = \frac{6\omega}{\pi c^2} \text{Im} [\hat{\mathbf{n}} \cdot \mathbf{G}(\mathbf{r}_0, \mathbf{r}_0, \omega) \cdot \hat{\mathbf{n}}] \quad (1)$$

where ω is the emitter characteristic frequency, $\hat{\mathbf{n}}$ is the unit vector in the direction of $\langle e|\mathbf{p}|g\rangle$ (where \mathbf{p} is the dipole operator), and $\mathbf{G}(\mathbf{r}, \mathbf{r}', \omega)$ is the Green function of the system. For a single boundary planar system, the Green function is available in the literature (see, for instance,²⁹), and for an isotropic

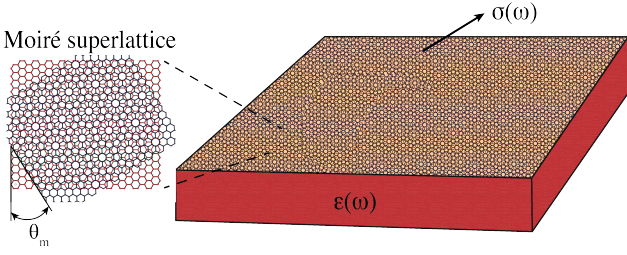


Figure 1. Our setup consists of a twisted bilayer of graphene on top of a substrate. The two layers of graphene are twisted by an angle θ_m , and the bilayer as a whole has a conductivity $\sigma(\omega)$. The substrate is characterized by a permittivity $\epsilon(\omega)$ that, for suspended TBGs, is equal to ϵ_0 .

emitter it is straightforward to show that $\rho = \rho_E + \rho_H$, where

$$\frac{\rho_E}{\rho_0} = \frac{1}{2} + \text{Re} \int_0^{k_0} dk_{\parallel} \frac{k_{\parallel} e^{2ik_{z0}z}}{4k_0 k_{z0}} \left[r_s + \left(\frac{2k_{\parallel}^2}{k_0^2} - 1 \right) r_p \right] + \text{Im} \int_{k_0}^{\infty} dk_{\parallel} \frac{k_{\parallel} e^{-2\kappa_{z0}z}}{4k_0 \kappa_{z0}} \left[r_s + \left(\frac{2k_{\parallel}^2}{k_0^2} - 1 \right) r_p \right] \quad (2)$$

and ρ_H is obtained from ρ_E by swapping $r_s \leftrightarrow r_p$. Here, $\rho_0 = k_{z0}^2/\pi^2 c$ is the free space density of states, $k_{z0} = \sqrt{k_0^2 - k_{\parallel}^2}$, $\kappa_{z0} = \sqrt{k_{\parallel}^2 - k_0^2}$, and $k_0 = \omega/c$ is the wavenumber. The 2nd term is associated to the contribution of propagating waves, as it can be seen from the fact that it is an integral over $k < k_0$, so k_{z0} is real. Conversely, the 3rd term is related to evanescent waves (in the z -direction), as $k_{z0} = i\kappa_{z0}$ is imaginary. Finally, the Fresnel reflection coefficients r_s, r_p , that owe their appearance in the Green function to the reflected modes on a plane, sharp boundary (the graphene sheet), are calculated by modeling the bilayer graphene as a surface density current at $z = 0$, resulting in²⁸

$$r_s = \frac{k_{z0} - k_{zs} - \mu_0 \omega \sigma}{k_{z0} + k_{zs} + \mu_0 \omega \sigma}, \quad r_p = \frac{\epsilon k_{z0} - k_{zs} + k_{z0} k_{zs} \sigma / \omega \epsilon_0}{\epsilon k_{z0} + k_{zs} + k_{z0} k_{zs} \sigma / \omega \epsilon_0}, \quad (3)$$

for $k_0 > k_{\parallel}$, and when $k_{\parallel} > k_0$ it is necessary to deal with the square roots appropriately. We have also $k_{zs} = \sqrt{\epsilon k_0^2 - k_{\parallel}^2}$, ϵ being the substrate's dielectric function, and σ is the 2D material conductivity.

The LDOS is a very useful quantity, first and foremost because it is directly proportional (in the weak coupling regime) to the spontaneous decay of a localized quantum emitter. Indeed, the spontaneous decay rate Γ_e (Γ_h) of an object with a transition electric (magnetic) dipole moment \mathbf{d}_e (\mathbf{d}_m) is given by Ref.^{29,30}

$$\Gamma_e = \frac{\pi \omega}{3 \hbar \epsilon_0} |\mathbf{d}_e|^2 \rho_e, \quad \Gamma_h = \frac{\pi \omega}{3 \hbar \epsilon_0} |\mathbf{d}_m|^2 \rho_h \quad (4)$$

In addition, the LDOS not only informs the total decay rate but also encodes valuable information about decay channels. By analysing the LDOS spectrum (i.e., its dependence on the transverse wave vector) it is possible to assess how likely certain type of waves are going to be excited (e.g., surface waves, or radiative waves).

B. Tight-binding model

Following some previous work on TBGs³¹, our tight-binding model is based on a linear combination of orthogonal p_z atomic orbitals. The Hamiltonian of a general multilayer system is written as:

$$H = - \sum_{i,j} t(\vec{R}_i - \vec{R}_j) |\vec{R}_i\rangle \langle \vec{R}_j| + H.c., \quad (5)$$

where $|\vec{R}_i\rangle$ represents the atomic orbital at site i and $t(\vec{R}_i - \vec{R}_j)$ is the hopping energy between orbitals i and j . Hopping energies t depend on interatomic distances and relative orientation between p_z orbitals at each site³¹:

$$-t(\vec{d}) = V_{pp\pi}(\vec{d}) \left[1 - \left(\frac{d_z}{d} \right)^2 \right] + V_{pp\sigma}(\vec{d}) \left(\frac{d_z}{d} \right)^2, \quad (6)$$

where the interatomic distance dependences of hopping energies are given by³¹:

$$V_{pp\pi}(\vec{d}) = V_{pp\pi}^0 \exp\left(-\frac{d - a_0}{\delta_0}\right) \quad (7)$$

$$V_{pp\sigma}(\vec{d}) = V_{pp\sigma}^0 \exp\left(-\frac{d - d_0}{\delta_0}\right), \quad (8)$$

where $\vec{d} = \vec{R}_i - \vec{R}_j$, $d_z = \vec{d} \cdot \hat{z}$, and $d = |\vec{d}|$. In our formalism, hopping between orbitals belonging to the same sheet are treated in the same footing as orbitals belonging to different sheets. We take $V_{pp\pi}^0 = -2.7$ eV and $V_{pp\sigma}^0 = -0.48$ eV to fit the dispersions of monolayer graphene and AB-stacked bilayer graphene. $a_0 = 0.142$ nm is the carbon-carbon nearest-neighbor distance, $d_0 = 0.335$ nm is the interlayer spacing, and δ_0 is the decay length of the hopping integral, chosen to be $0.184 a$, where $a = a_0 \sqrt{3}$, so that the next-nearest neighbor intralayer hopping becomes $0.1 V_{pp\pi}^0$. The hopping can be safely neglected for $d > 4a_0$.

C. Dynamical conductivity

The linear optical response of any electronic system is given by the optical conductivity. This conductivity is obtained from the sum of the two contributions: a regular conductivity ($\sigma_{\alpha\beta}^{reg}$) that describes interband transitions and a term containing the Drude weight ($D_{\alpha\beta}$) that is connected to the intraband processes. The total conductivity is given by

$$\sigma_{\alpha\beta}(\omega) = \frac{i D_{\alpha\beta}}{\hbar \omega + i\eta} + \sigma_{\alpha\beta}^{reg}(\omega), \quad (9)$$

where α and β are the different directions of the light polarization and η is a phenomenological broadening which is set to 3 meV. From the tight-binding model we can obtain the eigenfunctions and eigenenergies to calculate the Drude weight and regular conductivity. The Drude weight is given by³²

$$D_{\alpha\beta} = - \frac{e^2}{\hbar^2 S} \sum_{k,\lambda} \frac{\partial \epsilon_{k\lambda}}{\partial k_{\alpha}} \frac{\partial \epsilon_{k\lambda}}{\partial k_{\beta}} \frac{\partial f(\epsilon_{k\lambda})}{\partial \epsilon_{k\lambda}} \quad (10)$$

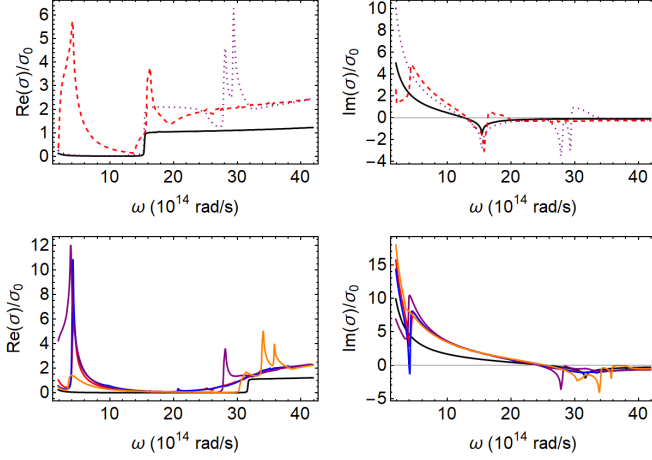


Figure 2. Upper plots: Real and imaginary parts of the optical conductivity of a suspended graphene monolayer (full black line), and suspended TBGs with $\theta_m = 7.34^\circ, 13.2^\circ$ (dashed red and dotted purple). The conductivities are normalized by $\sigma_0 = (4/\pi)(e^2/h)$. Temperature is set to zero and the chemical potential to $\mu = 0.5$ eV.

Lower plots: Same as above, but the suspended TBGs now have $\theta_m = 7.34^\circ, 9.46^\circ, 13.2^\circ, 16.9^\circ$ (red, blue, purple, orange; colors online), Temperature is also zero but the chemical potential is set at $\mu = 1$ eV.

where $\epsilon_{\vec{k}\lambda}$ are the band energies, $f(\epsilon)$ is the Fermi-Dirac distribution function, and S is the area of the system. Using the Kubo-Greenwood formula, the regular conductivity is found to be³¹

$$\sigma_{ii}^{reg}(\omega) = \frac{e^2 \hbar}{iS} \sum_{\vec{k}, \lambda, \lambda'} \frac{f(\epsilon_{\vec{k}\lambda}) - f(\epsilon_{\vec{k}\lambda'})}{\epsilon_{\vec{k}\lambda} - \epsilon_{\vec{k}\lambda'}} \frac{|\langle \lambda | v_i | \lambda' \rangle|^2}{\epsilon_{\vec{k}\lambda} - \epsilon_{\vec{k}\lambda'} + \hbar\omega + i\eta},$$

$$\sigma_{ij}^{reg}(\omega) \approx 0 \quad (11)$$

where $(i, j = 1, 2)$, $|\lambda\rangle$ is the eigenstate associated to $\epsilon_{\vec{k}\lambda}$ and $v_i = -\frac{i}{\hbar}[r_i, H]$ is the i -th component of the velocity operator. Matrix elements of the velocity operator in the tight-binding basis are given by³³

$$\langle \vec{R}_i | v | \vec{R}_j \rangle = \frac{i}{\hbar} \langle \vec{R}_i | H | \vec{R}_j \rangle \langle \vec{R}_i | r | \vec{R}_j \rangle \approx \frac{i}{\hbar} \langle \vec{R}_i | H | \vec{R}_j \rangle (\vec{R}_i - \vec{R}_j). \quad (12)$$

Our results for the optical conductivity are written in terms of $\sigma_0 = (4/\pi)(e^2/h)$, which is the universal dynamical conductivity of monolayer graphene. In Fig. 2 we present the conductivities for bilayer graphene twisted in three different angles, alongside the conductivity for a single graphene monolayer. It is patently clear that the conductivities of the TBGs have a much richer structure than the single monolayer: the peaks in the real part signal the presence of optical transitions between van Hove singularities³⁴. Remarkably, these transitions can be tuned by varying the twist angle, thus unveiling an alternative mechanism to control quantum emission in TBGs.

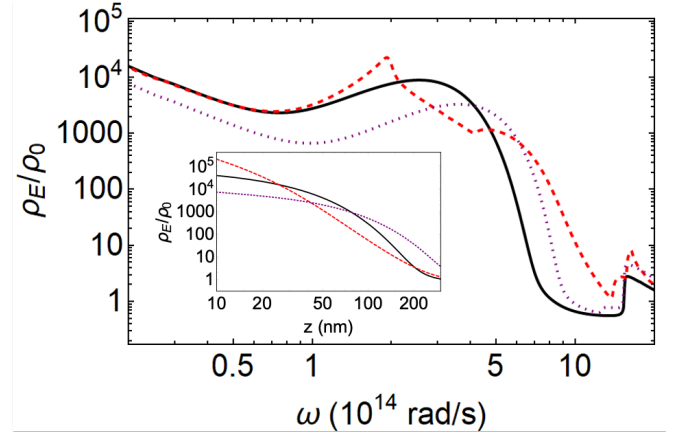


Figure 3. Electric contribution to the photonic local density of states at $\mu = 0.5$ eV, as a function of frequency, for a graphene monolayer (full black line), and bilayer graphene with $\theta_m = 7.34^\circ, 13.2^\circ$ (dashed red and dotted purple, respectively). The distance is fixed at $z = 30$ nm. The inset shows the distance dependence of the photonic LDOS for the same Moiré angles as in the main panel for $\omega = 2 \times 10^{14}$ rad/s.

III. RESULTS AND DISCUSSIONS

Once the conductivity of the TBG is known, one can straightforwardly obtain the reflection coefficients (3) and thus the electric and magnetic densities of states ρ_E and ρ_H . In Figs. 3 and 4 we depict the electric LDOS as a function of frequency, for suspended monolayer and bilayers with selected angles of twist, setting the chemical potential μ at 0.5 eV in Fig. 3 and 1 eV in Fig. 4. Despite presenting the same general structure, the two plots have peculiarities that deserve specific consideration.

The most prominent feature of the plot in Fig. 3 is the peak that arises for $\theta = 7.34^\circ$ at $\omega \approx 2 \cdot 10^{14}$ rad/s. In order to properly understand that, a small digression is necessary. Given that we are evaluating the LDOS at $z = 30$ nm, we have $\kappa_c := 1/z \approx 3.3 \cdot 10^7 \text{ m}^{-1} \gg k_0 \approx 6.7 \cdot 10^5 \text{ m}^{-1}$, so that the evanescent part largely dominates the local density of states in that frequency range. By isolating their contribution in (2), we get

$$\frac{\rho_E^{Eva}}{\rho_0} = \text{Im} \int_{k_0}^{\infty} dk_{\parallel} \frac{k_{\parallel} e^{-2\kappa_c z}}{4k_0 \kappa_c z} \left[r_s + \left(\frac{2k_{\parallel}^2}{k_0^2} - 1 \right) r_p \right]. \quad (13)$$

We see then that the LDOS is essentially controlled by the imaginary parts of r_s and r_p , which in turn are determined by the relation between the real and imaginary parts of the mono/bilayers' conductivities. If $|\text{Im}(\sigma)| \gg \text{Re}(\sigma)$, i.e., small losses, it is possible to show that, in the evanescent region, $\text{Im}(r_s), \text{Im}(r_p) \ll 1$ (see appendix) except in the vicinities of the surface plasmon polariton (SPP) dispersion relation, defined by the pole of r_p .

	$\sigma(\omega_1)/\sigma_0$ ($\mu = 0.5$ eV)	$\sigma(\omega_2)/\sigma_0$ ($\mu = 1$ eV)
Mono	$0.09 + 3.82 i$	$0.31 + 10.11 i$
$\theta_m = 7.34^\circ$	$0.78 + 1.22 i$	$1.23 + 16.10 i$
$\theta_m = 9.46^\circ$		$0.69 + 14.90 i$
$\theta_m = 13.2^\circ$	$0.18 + 7.65 i$	$1.92 + 6.74 i$
$\theta_m = 16.9^\circ$		$0.58 + 18.43 i$

Table I. Values of the conductivities for selected twisted bilayers. The frequency values are $\omega_1 = 2 \cdot 10^{14}$ rad/s and $\omega_2 = 1.5 \cdot 10^{14}$ rad/s, and $\sigma_0 = e^2/4\hbar$. For comparison, we show also the values for a graphene monolayer.

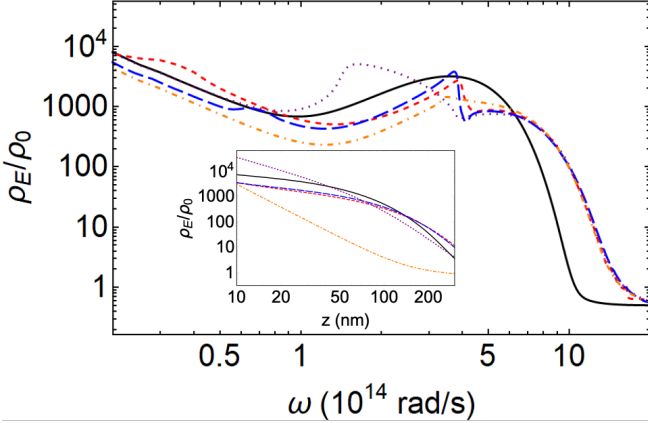


Figure 4. Electric contribution to the photonic local density of states at $\mu = 1$ eV, as a function of frequency, for a graphene monolayer (full black line), and bilayer graphene with $\theta_m = 7.34^\circ, 9.46^\circ, 13.2^\circ, 16.9^\circ$ (dashed red, long-dashed blue, dotted purple, and dot-dashed orange respectively). As in Fig 3, the distance is fixed at $z = 30$ nm. The inset shows the distance dependence of the photonic LDOS for the same Moiré angles as in the main panel for $\omega = 2 \times 10^{14}$ rad/s.

Bearing that in mind, we can end our digression and, in order to understand the underlying physics of quantum emission in TBG, plot in Fig. 5 the integrand of the LDOS for $\omega = 2 \cdot 10^{14}$ rad/s. The sharp peaks we see in the full black and dotted purple curves are the respective SPPs, indicating that if an emitter (in that frequency) is placed at ≈ 30 nm from a monolayer or the $\theta_m = 13.2^\circ$ bilayer, it would most likely decay by exciting SPPs in the layers. In addition, the peaks are so sharp that, in all those 3 cases, expression (13) may be very well approximated by an opportune application of the Cauchy residue theorem, yielding

$$\frac{\rho_E^{\text{Eva}}}{\rho_0} \approx \frac{\pi}{k_0^3} \text{Re} [k_{\text{spp}}^3 e^{-2k_{\text{spp}}z}], \quad (14)$$

where $k_{\text{spp}} = 2i\omega\epsilon_0/\sigma$, and we used that $k_{\text{spp}} \gg k_0$.

However, if the real and imaginary parts of the mono/bilayer conductivities are comparable (higher losses), the physical scenario becomes different. The SPP pole moves away from the real axis and the behaviour of the integrand in (13) becomes much smoother, allowing us to neglect the SPP contribution and simply integrate over the evanescent region

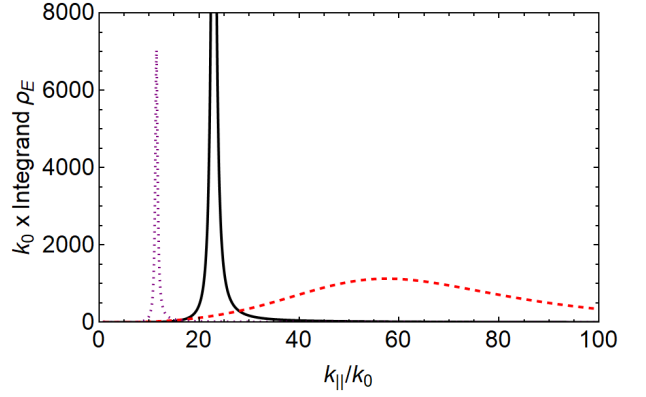


Figure 5. The integrand of the electric LDOS as function of $k_{||}$, for a monolayer (solid black) and twisted bilayers of 7.34° (dashed red) and 13.2° (dotted purple). One can immediately see the SPP signatures as sharp peaks for the latter 2 TBGs and the monolayer, while the 7.34° TBG is dominated by lossy surface waves. See text for further discussion.

(or, as defined by Ford and Weber³⁵, over the lossy surface waves - LSW). In the $k_{||} \gg k_0$ approximation, we get

$$\frac{\rho_E^{\text{Eva}}}{\rho_0} \approx \frac{1}{2k_0^3} \int_0^\infty dk_{||} k_{||} \text{Im}(r_p) e^{-2k_{||}z} = \frac{1}{8(k_0z)^2} \frac{\text{Im}(k_{\text{spp}})}{k_0} \quad (15)$$

We clearly see this smoother behaviour in the dashed red curve in Fig. 5, for $\theta_m = 7.34^\circ$. We have then two competing mechanisms to increase the LDOS: the SPP channel for a low-loss situation, and the LSW channel when higher losses are present. In the first case - the full, dotted, large-dashed curves - the LDOS has this exponential behaviour (typical of SPP interactions) but in the $k_{\text{spp}}z \ll 1$ limit (that always holds here) we conclude that it essentially grows with k_{spp} , and that is why in Fig. 5 we see that the peaks get larger as their centres move to the right in the horizontal axis. However, even the contribution of the monolayer's very high peak to the LDOS is much smaller than that of the lower but much wider $\theta_m = 7.34^\circ$ bilayer, which is ultimately connected to the fact that the LDOS of the latter is ruled by the power law behavior shown in (15). This means that, provided $\text{Im} k_{\text{spp}}$ is not negligible, it gets very large in the limit $k_0z \ll 1$. The condition upon k_{spp} is assured by striking a balance between the real and imaginary parts of σ , and this has a clear physical interpretation: the role of losses is to add these dissipative quasi-modes to the LDOS (so that the red dashed curve is way wider than the others), but too much loss quenches the contribution of each mode, overcoming the effect of having more modes available. The optimal situation is then reached when $\text{Im} \sigma \gtrsim \text{Re} \sigma$ - see table I - explaining the huge enhancement of the LDOS in this case.

We can now set our sights in the results of Fig. 4, that is, for $\mu = 1$ eV. This time around we have a softened peak at $\omega \approx 1.5 \cdot 10^{14}$ rad/s for $\theta = 13.2^\circ$, which occurs for the same reasons already discussed in the previous paragraph. Here we shall focus on the quite sharp step just shy of $4 \cdot 10^{14}$ rad/s,

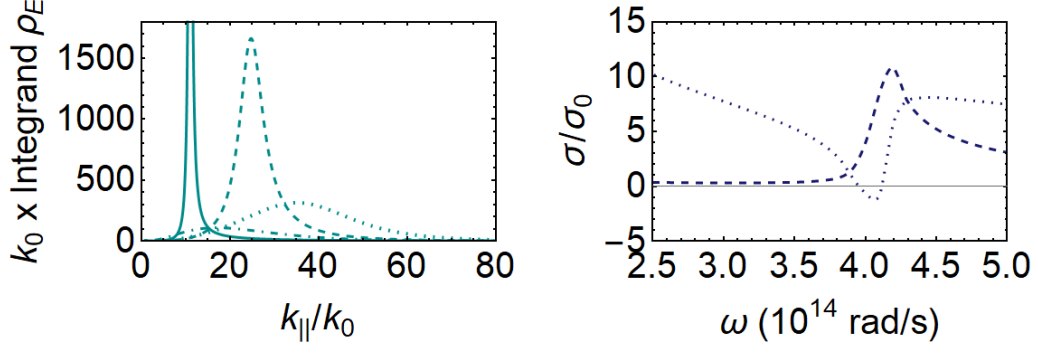


Figure 6. Left plot: the LDOS of the $\theta = 9.46^\circ$ TBG at four different frequencies, $\omega = 3 \cdot 10^{14}$ rad/s (solid line), $3.7 \cdot 10^{14}$ rad/s (dashed line), $3.85 \cdot 10^{14}$ rad/s (dotted line), $4 \cdot 10^{14}$ rad/s (dot-dashed line). Right plot: Real (dashed line) and imaginary (dotted line) parts of the conductivity of $\theta = 9.46^\circ$ TBG. In the two plots we set $\mu = 1$ eV.

most prominently shown in the TBG of $\theta = 9.46^\circ$. This is due to a sudden disappearance of a marked surface plasmon-polariton as we approach $\omega = 4 \cdot 10^{14}$ rad/s from below: in the left plot of Fig. 6 we depict the behaviour of the LDOS' integrand for different frequencies. For $\omega = 3 \cdot 10^{14}$ rad/s (solid line) we have a very sharp SPP but at the onset of the near discontinuity occurring at $3.7 \cdot 10^{14}$ rad/s (dashed line), the SPP is already somewhat broadened, despite the fact it is still quite prominent. However, at $3.85 \cdot 10^{14}$ rad/s (dotted line) we see that the peak is so wide that it hardly makes sense to still talk about a SPPs, and it is virtually nonexistent for $4 \cdot 10^{14}$ rad/s (dot-dashed line). These results are better appreciated by recovering the data for the conductivity, as we do in the right plot of Fig. 6: while the conductivity has a significant positive imaginary part (and negligible real part) we have a strong surface plasmon-polariton, as expected. We hit the (local) maximum value for the LDOS around $3.7 \cdot 10^{14}$ rad/s - where, again, $\text{Im } \sigma \gtrsim \text{Re } \sigma$ - and as $\text{Im } \sigma$ crosses the real part and even becomes negative, the SPP channel is strongly suppressed, and with it the whole local density of states.

IV. CONCLUSIONS

We have theoretically investigated the local density of states (LDOS) of twisted bilayer graphene (TBG) and its potential applications to tailor quantum emission. We have shown that, due to the remarkable structure that the Moiré patterns allow in the conductivity, calculated using the tight-binding method, the LDOS can be drastically altered by up to two orders of magnitude when the Moiré angle is varied. This large variation is physically explained in terms of the strong dependence of the surface plasmon-polariton structure upon the Moiré angle. By investigating the dependence of the LDOS on the Moiré angle, frequency, and chemical potential, we identify the ideal scenario for significantly enhancing the LDOS, which can be achieved by a balance between the real and imaginary parts of the TBG conductivity. In practice, this optimal amount of loss could be realized by, for in-

stance, incorporating gain in the system as it has been implemented in graphene-based photonic devices³⁶. Finally we have shown that the LDOS for certain TBGs may present a very sharp dependence on frequency, also related to the appearance/disappearance of SPPs, allowing for tuning the LDOS in a broad spectral range. Our results disclose the full potential of TBG as an alternative, versatile system for controlling spontaneous emission and enhancing light-matter interactions, and hopefully will foster further nanophotonics applications in other 2D Moiré materials.

V. ACKNOWLEDGEMENTS

F.J.C., F.S.S.R., C.F., R.B.C. and F.A.P. acknowledge Conselho Nacional de Desenvolvimento Científico e Tecnológico and Fundação de Amparo a Pesquisa do Estado do Rio de Janeiro for financial support. W.K.-K acknowledges the Laboratory Directed Research and Development program of Los Alamos National Laboratory for funding under the project 20190574ECCR.

VI. APPENDIX

For suspended graphene, meaning $\epsilon = 1$, we have (in the evanescent region)

$$\begin{aligned} \text{Im}(r_p) &= \text{Im} \left[\frac{i\sigma/(2\omega\epsilon_0)}{1/\kappa_{z0} + i\sigma/(2\omega\epsilon_0)} \right] \\ &= \frac{\sigma_R/(2\omega\epsilon_0\kappa_{z0})}{1/\kappa_{z0}^2 + 2\sigma_I/(2\omega\epsilon_0\kappa_{z0}) + \sigma\sigma^*/(2\omega\epsilon_0)^2} \quad (16) \end{aligned}$$

where $\sigma_R = \text{Re}(\sigma)$ and $\sigma_I = \text{Im}(\sigma)$. Using 10^{-3} S/m $\approx 2\sigma_0$ as a typical value for $|\sigma|$ and also the small losses condition ($\sigma_I \gg \sigma_R$), we get

$$\text{Im}(r_p) \approx \frac{\sigma_R}{\sigma_I} \frac{2\omega\epsilon_0}{\sigma_I \kappa_{z0}} \approx \frac{5.3}{\kappa_{z0}} \frac{\sigma_R}{\sigma_I}, \quad (17)$$

where we chose $\omega = 3 \cdot 10^{14}$ rad/s and κ_{z0} is measured in $(\mu\text{m})^{-1}$. Therefore, we see that, except very close to $\kappa_{z0} = 0$,

$\text{Im}(r_p) \ll 1$ is easily satisfied.

The reasoning for $\text{Im}(r_s)$ is totally analogous.

* kortkamp@lanl.gov

† culchac@if.ufrj.br

- ¹ A. H. Castro Neto, F. Guinea, N. M. R. Peres, K. S. Novoselov, and A. K. Geim Rev. Mod. Phys. **81**, 109 (2009).
- ² A. K. Geim and I. V. Grigorieva, Nature **499**, 419 (2013).
- ³ J. M. B. Lopes dos Santos, N. M. R. Peres, and A. H. Castro Neto, Phys. Rev. Lett. **99**, 256802 (2007).
- ⁴ Xuesong Li, Weiwei Cai, Jinho An, Seyoung Kim, Junghyo Nah, Dongxing Yang, Richard Piner, Aruna Velamakanni, Inhwa Jung, Emanuel Tutuc, Sanjay K. Banerjee, Luigi Colombo and Rodney S. Ruoff, Science **324**,1312 (2009).
- ⁵ Chun-Chieh Lu, Yung-Chang Lin, Zheng Liu, Chao-Hui Yeh, Kazu Suenaga, and Po-Wen Chiu, ACS Nano **7**, 2587 (2013).
- ⁶ Shu Nie, Andrew L. Walter, Norman C. Bartelt, Elena Starodub, Aaron Bostwick, Eli Rotenberg, and Kevin F. McCarty, ACS Nano **5**, 2298 (2011).
- ⁷ Guohong Li, A. Luican, J. M. B. Lopes dos Santos, A. H. Castro Neto, A. Reina, J. Kong and E. Y. Andrei, Nature Phys. **6**, 109 (2010).
- ⁸ V. Carozo, C. M. Almeida, B. Fragneaud, P. M. Bedê, M. V. O. Moutinho, J. Ribeiro-Soares, N. F. Andrade, A. G. Souza Filho, M. J. S. Matos, B. Wang, M. Terrones, Rodrigo B. Capaz, A. Jorio, C. A. Achete, and L. G. Cançado, Phys. Rev. B **88**, 085401 (2013).
- ⁹ Kyoungwhan Kim, Matthew Yankowitz, Babak Fallahazad, Sangwoo Kang, Hema C. P. Movva, Shengqiang Huang, Stefano Larentis, Chris M. Corbet, Takashi Taniguchi, Kenji Watanabe, Sanjay K. Banerjee, Brian J. LeRoy, and Emanuel Tutuc, Nano Lett. **16**, 1989 (2016).
- ¹⁰ A. Luican, Guohong Li, A. Reina, J. Kong, R. R. Nair, K. S. Novoselov, A. K. Geim, and E. Y. Andrei Phys. Rev. Lett. **106**, 126802 (2011).
- ¹¹ Wei Yan, Mengxi Liu, Rui-Fen Dou, Lan Meng, Lei Feng, Zhao-Dong Chu, Yanfeng Zhang, Zhongfan Liu, Jia-Cai Nie, and Lin He, Phys. Rev. Lett. **109**, 126801 (2012).
- ¹² Long-Jing Yin, Jia-Bin Qiao, Wei-Jie Zuo, Wen-Tian Li, and Lin He, Phys. Rev. B **92**, 081406(R) (2015).
- ¹³ Y. Cao, V. Fatemi, S. Fang, K. Watanabe, T. Taniguchi, E. Kaxiras, and P. Jarillo-Herrero, Nature **556**, 43 (2018).
- ¹⁴ Y. Cao, V. Fatemi, A. Demir, S. Fang, S. L. Tomarken, J. Y. Luo, J. D. Sanchez-Yamagishi, K. Watanabe, T. Taniguchi, E. Kaxiras, R. C. Ashoori, and P. Jarillo-Herrero, Nature **556**, 80 (2018).
- ¹⁵ E. Koren, I. Leven, E. Lartscher, A. Knoll, O. Hod, and U. Duerig, Nat. Nanotechnol. **11**, 752 (2016).
- ¹⁶ T. Chari, R. Ribeiro-Palau, C. R. Dean, and K. Shepard, Nano Lett. **16**, 4477 (2016).
- ¹⁷ Kyle L. Seyler, Pasqual Rivera, Hongyi Yu, Nathan P. Wilson, Essance L. Ray, David G. Mandrus, Jiaqiang Yan, Wang Yao and Xiaodong Xu, Nature **567**, 66 (2019).
- ¹⁸ Evgeny M. Alexeev, David A. Ruiz-Tijerina, Mark Danovich, Matthew J. Hamer, Daniel J. Terry, Pramoda K. Nayak, Seongjoon Ahn, Sangyeon Pak, Juwon Lee, Jung Inn Sohn, *et al.*, Nature **567**, 81 (2019).
- ¹⁹ Kha Tran, Galan Moody, Fengcheng Wu, Xiaobo Lu, Junho Choi, Kyoungwhan Kim, Amritesh Rai, Daniel A. Sanchez, Jiamin Quan, Akshay Singh, *et al.*, Nature **567**, 71 (2019).
- ²⁰ Chenhao Jin, Emma C. Regan, Aiming Yan, M. Iqbal Bakti Utama, Danqing Wang, Sihan Zhao, Ying Qin, Sijie Yang, Zhiren Zheng, Shenyang Shi, Kenji Watanabe, Takashi Taniguchi, Se-faattin Tongay, Alex Zettl and Feng Wang, Nature **567**, 76 (2019).
- ²¹ H. Yu, G.-B. Liu, J. Tang, X. Xu, W. Yao, Sci. Adv. **3**, e1701696 (2017).
- ²² C. Chakraborty, N. Vamivakas, and D. Englund, Nanophotonics **8**, 2017 (2019).
- ²³ F. J. García de Abajo, ACS Photonics **1**,135 (2014).
- ²⁴ F. H. L. Koppens, D. E. Chang, and F. García de Abajo, Nano Lett. **11**, 3370 (2011).
- ²⁵ L. Gaudreau, K. J. Tielrooij, G. E. D. K. Prawiroatmodjo, J. Osmond, F. J. García de Abajo, and F. H. L. Koppens, Nano Lett. **13**, 2030 (2013).
- ²⁶ P. A. Huidobro, A. Y. Nikitin, C. González-Ballesterro, L. Martín-Moreno, and F. J. García-Vidal Phys. Rev. B **85**, 155438 (2012)
- ²⁷ K. J. Tielrooij, L. Orona, A. Ferrier, M. Badioli, G. Navickaite, S. Coop, S. Nanot, B. Kalinic, T. Cesca, L. Gaudreau *et al.*, Nature Physics **11**, 281 (2015).
- ²⁸ W. J. M. Kort-Kamp, B. Amorim, G. Bastos, F. A. Pinheiro, F. S. S. Rosa, N. M. R. Peres, and C. Farina Phys. Rev. B **92**, 205415 (2015).
- ²⁹ L. Novotny and B. Hecht, *Principles of nano-optics*, Cambridge university press (2012).
- ³⁰ R. Carminati, A. Caze, D. Cao, F. Peragut, V. Krachmalnicoff, R. Pierrat, Y. De Wilde, Surface Science Reports, **7**, 1 (2015).
- ³¹ Pilkyung Moon and Mikito Koshino. Phys. Rev. B **87**, 205404, (2013).
- ³² G. B. Ventura, D. J. Passos, J. M. B. Lopes dos Santos, J. M. Viana Parente Lopes, and N. M. R. Peres Phys. Rev. B **96**, 035431, (2017).
- ³³ L. Brey and C. Tejedor. Solid State Commun., **48**, 403-406, 1983.
- ³⁴ Adriana Vela, M. V. O. Moutinho, F. J. Culchac, P. Venezuela, and Rodrigo B. Capaz, Phys. Rev. B **98**, 155135 (2018).
- ³⁵ G. W. Ford, and W. H. Weber, Phys. Rep. **113** 195 (1984).
- ³⁶ Lijun Meng, Ding Zhao, Yuanqing Yang, F. Javier García de Abajo, Qiang Li, Zhichao Ruan, and Min Qiu Phys. Rev. Applied **11**, 044030 (2019).